J Comput Aided Mol Des (2014) 28:1077–1091
DOI 10.1007/s10822-014-9786-3

A QM/MM study of the associative mechanism for the phosphorylation reaction catalyzed by protein kinase A and its D166A mutant

Ayax Pérez-Gallegos · Mireia Garcia-Viloca · Àngels González-Lafont · José M. Lluch

Received: 15 May 2014 / Accepted: 7 August 2014 / Published online: 17 August 2014

Abstract Here we analyze in detail the possible catalytic role of the associative mechanism in the γ-phosphoryl transfer reaction in the catalytic subunit of the mammalian cyclic AMP-dependent protein kinase (PKA) enzyme and its D166A mutant. We have used a complete solvated model of the ATP-Mg_2-Kemptide/PKA system and good levels of theory (B3LYP/MM and MP2/MM) to determine several potential energy paths from different MD snapshots, and we present a deep analysis of the interaction distances and energies between ligands, metals and enzyme residues. We have also tested the electrostatic stabilization of the transition state structures localized herein with the charge balance hypothesis. Overall, the results obtained in this work reopen the discussion about the plausibility of the associative reaction pathway and highlight the proposed role of the catalytic triad Asp166–Lys168–Thr201.

Keywords Enzyme catalysis · Enzyme models · Protein kinase · QM/MM calculations · Reaction mechanisms

Introduction

Protein phosphorylation is a ubiquitous regulatory mechanism in both eukaryotes and prokaryotes. Abnormal phosphorylation turns out to be a cause or consequence of several diseases and, for that reason, the enzymes that control this process, protein kinases and phosphatases, have become important targets for rational drug design [1]. Protein kinases are a large super family of phosphoryl transferases that represent one of the fundamental components of cell-signaling pathways in all organisms [2–4]. Those enzymes catalyze the transfer of the γ-phosphoryl group of ATP to the hydroxyl side chain of specific serine, threonine or tyrosine residues in their target proteins with the assistance of Mg^{2+} ions. In fact, the human kinome (the collection of all human kinases) accounts for approximately 2 % of the entire genome and therefore encompasses the largest family of enzymes [5]. Among over 2,000 unique eukaryotic protein kinases, cyclic-adenosine monophosphate (cAMP)-dependent protein kinase (PKA) is the best characterized member and often serves as a prototypical enzyme for the whole family [6–8]. The inactive PKA holoenzyme is a tetramer composed of two regulatory and two catalytic subunits (PKA-C) that become dissociated following the binding of the two messenger cAMP molecules to the regulatory subunits. Once the two catalytic subunits become dissociated, they work independently.

The bean-shaped fold for PKA-C is highly conserved with two lobes (small and large). The active site of this enzyme is located at the interface of the two lobes forming a deep cleft. The triphosphate arm of ATP, the Mg^{2+} ions, and the peptide/protein substrate are located at the entrance of that cavity where the phosphoryl-transfer reaction takes place whereas the nucleoside moiety of ATP is completely buried in this cavity [9]. Recent NMR studies show how binding of the nucleotide acts to dynamically couple the two lobes making it "committed" to catalysis [10].

The catalytic cycle of an active protein kinase is comprised of the binding of ATP·Mg^{2+}, the second magnesium ion in those kinases that require two divalent metal ions for optimum catalysis [11, 12], and protein substrate, followed

A. Pérez-Gallegos · M. Garcia-Viloca · À. González-Lafont (✉) · J. M. Lluch
Departament de Química, Institut de Biotecnologia i de Biomedicina, Universitat Autònoma de Barcelona, 08193 Bellaterra, Barcelona, Spain
e-mail: angels@klingon.uab.es; Angels.Gonzalez@uab.cat

by the chemical step of phosphoryl transfer, and finally product release. Solvent viscosity effect studies of the fully activated states of many kinases, including PKA, have shown that product release is often rate-limiting [13]. However, despite extensive experimental and computational studies of PKA, there are still many open questions about the mechanistic details of catalysis for PKA or kinases in general. In fact, very recently it has been shown that one of the magnesium ions remains in the active site following complete phosphoryl transfer while the other one is expelled as an important part of the rate-limiting ADP release [14, 15].

On the basis of the conserved catalytic core, it is believed that protein kinases share a common phosphoryl-transfer mechanism, although several detailed aspects remain unsettled [16, 17]. The transition states of that phosphoryl-transfer reaction have been traditionally classified as associative or dissociative transition states. In the associative mechanism a trigonal bipyramidal transition state is formed in which the bond formation with the substrate serine/threonine or tyrosine residue begins before the bond between β and γ-phosphate is completely broken. In contrast, the dissociative mechanism involves a complete break in the leaving group yielding a metaphosphate before the new bond with the nucleophilic serine/threonine or tyrosine is being formed [18–20].

The most detailed model for the phosphoryl-transfer transition state conformation of a protein kinase is the AlF_3 transition state analog (TSA) of PKA (1L3R) [21], however several other crystal structures of PKA in complexes with substrate/inhibitory peptides and various nucleotides have turned out to be very useful to reveal the interactions between the enzyme and the substrates at different stages along the reaction pathway [22, 23]. Several conserved residues converge near the site of phosphoryl transfer and appear to play important catalytic functions (See Fig. 1). Asp184 is a strictly conserved residue of the "DGF" motif, nearly invariant in protein kinases, that interacts with the Mg^{2+} ion which chelates the β- and γ-phosphates of ATP. In this way, the terminal phosphate is better positioned for direct transfer to the hydroxyl acceptor and the charge of the γ-phosphate is masked limiting electrostatic repulsion for an incoming nucleophile [5]. Additional stabilization of the phosphates emanate from the interaction of Lys72 with the α- and β-phosphates of ATP. Mutagenesis studies on this conserved lysine indicate that its primary function is to facilitate phosphoryl group transfer without influencing ATP binding [24]. On the other hand, there are intriguing questions concerning the roles of Asp166 and Lys168 residues [4]. In several X-ray crystallographic structures, the carboxylate group of Asp166 was found near the hydroxyl proton of the peptide substrate [25, 26]. That experimental finding was used as evidence to support a general-base catalysis via H-transfer from the peptide substrate to Asp166. Moreover, mutagenesis experiments performed at high magnesium concentrations showed a 370-fold reduction in k_{cat} of yeast Asp210Ala mutant and a negligible activity in Asp149Ala PhK mutant (corresponding to Asp166 in mammalian PKA), [24, 27] confirming that the conserved aspartate is clearly important for efficient catalysis. The experimental hypothesis was then that Asp166 could either help to correctly orient the reactants or act as a proton acceptor late in the reaction process according to the dissociative mechanism. Lys 168 in PKA interacts electrostatically with the γ-phosphate, but this interaction is not fully conserved throughout the enzyme family. In PKA, Lys168 also interacts with Thr201, a residue that forms part of the P + 1 binding cleft. In yeast PKA, replacement of this lysine with alanine leads to a 30-fold elevated K_M for Kemptide and a 50-fold reduced k_{cat} [24].

From a theoretical point of view, early semiempirical quantum mechanical (QM) calculations on cluster models of the enzyme-ATP-substrate complex, or semiempirical quantum mechanics/molecular mechanics (QM/MM) calculations on complete models of the biological system, gave results that support the associative mechanism, without any major role of Asp166 [28–30]. However, the inadequacy of semiempirical methods that lack d-orbitals to study phosphoryl-transfer reactions was demonstrated. Then, the exploration of the potential energy surface for the phosphoryl-transfer reaction was carried out by other authors with higher QM levels of theory on cluster or complete models of the system [19, 31–33]. These later theoretical studies are consistent with the role of Asp166 as a proton-trap late in the reaction process corresponding to a dissociative mechanism. Thus Valiev et al. [19] carried out B3LYP calculations on a cluster including all of the essential conserved residues and a molecule of ethanol to represent the Ser substrate. Diaz and Field [32] performed B3LYP calculations on a cluster including the 20-residue peptide model substrate built based on the 20-residue peptide inhibitor PKI (5–24) located in the kinase active site in the 1CDK crystallographic structure. In turn, in two recent studies by Cheng et al. [18, 33] a B3LYP/MM potential energy surface was explored for a complete enzyme-Mg_2–ATP-substrate complex starting from the 1L3R and 1ATP crystallographic structures; the substrate peptide SP20 was used. Finally, Valiev et al. [31] have carried out free energy calculations by combining a B3LYP/MM reaction path with appropriate MM molecular dynamics simulations along that reaction path on the complete system; the starting structure for the calculations was taken from the 1ATP crystallographic structure and the substrate peptide SP20 was used. Only in the work by Diaz and Field [32] using a cluster model the associative

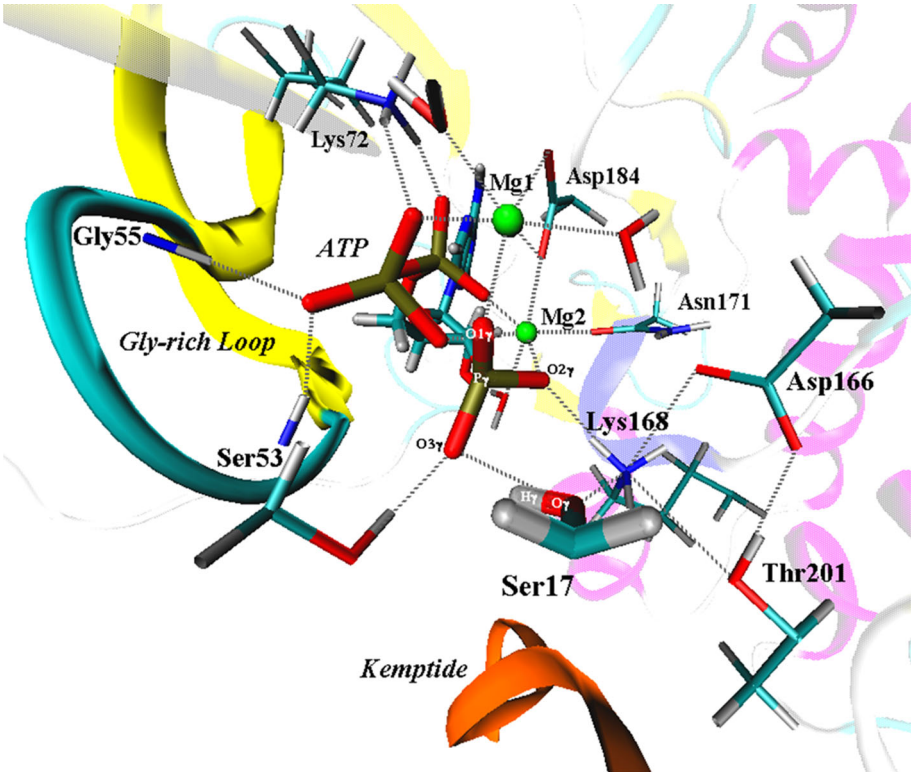

Fig. 1 Schematic representation of the most important interactions within the PKA active site

mechanism was analyzed and in that case it was discarded in front of the dissociative pathway.

In a previous work, we carried out a theoretical study of the γ-phosphoryl group transfer of ATP to Ser17 of the model substrate Kemptide (LRRASLG) in PKA [34]. The two different crystallographic structures used in previous theoretical studies were selected: 1CDK and 1ATP, the first one is phosphorylated only on residue Thr197 whereas the second structure also has the residue Ser338 modified into a phosphoserine. The higher flexibility of 1CDK observed in our molecular dynamics simulations showed that the phosphorylation state of the enzyme can modify the dynamical behavior of the active biological system and the potential energy profile for the two mechanisms [20]. Thus, whereas the dissociative mechanism was found roughly equally fast for both structures at the B3LYP/6-31+G(d)//AM1/d-PhoT/MM level, only in 1CDK the associative mechanism was found viable. In a later work [35], we analyzed by means of molecular dynamics simulations of the 1CDK mutant D166A the effect of the presence and the absence of Asp166. Our molecular dynamics results clearly showed that the aspartate to alanine mutation led to the opposite effect than the one obtained when modeling a deactivated form (without any phosphorylated residue) of 1CDK. In fact, in the mutated enzyme the interaction between ATP and Ser17 becomes stronger than in the deactivated enzyme with the general disposition of the catalytic center resembling the associative mechanism prereactive state. Thus, as observed experimentally, the mutation does not completely deactivate the enzyme and the residual activity of the D166A mutant (0.4 % of the wild type activity) [24] can only be explained by the viability of the associative mechanism. In addition, other kinases have also been experimentally proposed to function by an associative mechanism [36, 37], and very recently the role of the associative mechanism in phosphate hydrolysis in solution has been highlighted and proposed to be also relevant for proteins [38].

Recently, the analysis of the catalytic mechanism of phosphoryl transfer from a basis of physical organic chemistry allied to enzyme biochemistry, and with a strong focus on the associative/dissociative nature of the reactions, is being complemented by structural studies. These studies juxtapose X-ray analysis with NMR spectroscopy allowing a new interpretation of the phosphoryl transfer mechanism [39]. This new perspective is focused on understanding how enzymes have solved the problem of phosphate charge repulsion of the attacking nucleophile. In this sense, the charge balance hypothesis (CBH) has been established as a general explanation on how phosphoryl transfer transition states are stabilized in several kinases (in particular, in PKA) [40].

The aim of the present paper is to analyze in detail the possible catalytic role of the associative mechanism in the phosphoryl transfer reaction in the mammalian PKA-C enzyme and its D166A mutant by using a complete

solvated model of the ATP-Mg_2-Kemptide/PKA system. We will use higher levels of QM/MM theory than the one employed in our previous work in which the proposal of the viability of that associative pathway was raised. In addition, an analysis of the associative transition states from the charge balance hypothesis perspective will be carried out theoretically with the purpose of comparing with recent experimental conclusions concerning transition state stabilization in this key protein kinase.

Models and methods

The initial structures for the study of the reactivity of the cAMP-dependent protein kinase (PKA) had been built from the structures generated during previous molecular dynamics (MD) simulations of the ternary Michaelis complex of the kinase with ATP-Mg_2 and the synthetic heptapeptide Kemptide as substrate [34]. Specifically, to build the former biological model, the starting coordinates of the enzyme's catalytic subunit were taken from the crystallographic structure with PDB-ID-code 1CDK [26], which corresponds to the closed active conformation of the enzyme and has the residue Thr197 modified into a phospho-threonine (pThr197).

Whether a frame along the referred MD simulations was geometrically appropriate to initiate the study of the associative mechanisms or not, was evaluated taking into account the O_γSer17–P_γATP distance and the position of the H_γSer17 relative to the Asp166 residue. In addition, to take into account in our study the strong Asp166–Thr201 interaction observed in substrate-bound complexes of PKA (which has even suggested the possibility that this interaction may be involved in the substrate recognition process), we also used that distance for defining the starting structures. Then: (1) values of 3.5 ± 0.2 Å for the O_γSer17–P_γATP together with an O_γSer17–H_γSer17–O_δ2Asp166 angle not higher than 150° (so that the H_γSer17 atom does not remain completely directed towards any of the two $O_\delta i$Asp166, distinctive feature of dissociative mechanism), were considered propitious to set up the initial structures in our simulations; and (2) from such set of selected structures, three initial $O_\delta i$Asp166–O_γThr201 values (3.0 ± 0.2, 3.7 ± 0.2 and 4.5 ± 0.3 Å) were considered representative to study the role of Thr201, and also of the Asp166–Lys168–Thr201 triad, in the geometry and energetics of the active site at the stationary points of the associative mechanism. Those structures, neither favoring nor excluding the associative mechanism, kept $Ser17^{Kemptide}$ and γ-phosphoryl group moieties close enough of each other so that it was possible to start modeling both the S_N2-type reaction and its concomitant proton transfer reaction between moieties here involved.

Within the reported free 6 ns MD simulation (structural data was recorded for subsequent analysis every 0.05 ns) [34], the geometrical requirements indicated in the previous paragraph were fulfilled on frames, so named, eq21 (MD-snapshot at 1.05 ns; 3.0 ± 0.2 Å or short $O_\delta i$Asp166–O_γThr201 interaction), eq55 (MD-snapshot at 2.75 ns; 3.7 ± 0.2 Å or intermediate $O_\delta i$Asp166–O_γThr201 interaction) and eq91 (MD-snapshot at 4.55 ns; 4.5 ± 0.3 Å or long $O_\delta i$Asp166–O_γThr201 interaction), which clearly correspond, respectively, to the initial, middle and final part of the MD simulation. In addition, we also used a 1CDK-Kemptide reactant Michaelis complex geometry defined in a previous work within our group [20], which presented a suitable –almost specific– configuration for the associative mechanism (2.7 Å for the O_γSer17–P_γATP distance and the H_γSer17 directed towards the influence area of γ-phosphoryl oxygen atoms, resulting in a small O_γSer17–H_γSer17–$O_\delta i$Asp166 angle of 66°). In this case, the system has a long $O_\delta i$Asp166–O_γThr201 distance (4.8 Å), but the Thr201 residue side-chain remains close to the Ser17 and Lys168 residue side-chains involved in the reaction core (being O_γSer17–O_γThr201 and N_ζLys168–O_γThr201 distances 3.2 and 3.4 Å, respectively). Henceforth, we will refer to this geometry as M1.

From the selected geometries, we have deleted all the water molecules outside a 25 Å radius sphere, centered on the geometric center of O_γSer17, $O3_\gamma$ATP, and O_δ2-Asp166. Furthermore, all residues and water molecules within 20 Å of such point were included in the optimization process as the active region, allowed to move freely, while the remaining atoms were kept frozen in their positions along the subsequent calculations. The number of free atoms in eq21, eq55, eq91 and M1 is 5,663, 5,607, 5,537 and 5,537, respectively; while the number of fixed atoms is 3,002, 2,964, 2,714 and, 3,074, respectively. These fractioned systems served as starting points for the QM/MM calculations.

QM/MM calculations were performed with the modular program package ChemShell [41], using TURBOMOLE [42] to obtain the quantum mechanical (QM) energies and gradients. Specifically, the Schrödinger equation for the QM region was solved based on a local basis implementation of density functional theory with the B3LYP [43–48] approximation for the exchange–correlation functional and expanding wave-functions by means of Pople's 6-31+G(d) basis set. The remainder of the protein was described at the molecular mechanics (MM) level. The energies and gradients for the MM region were evaluated by DL_POLY [49], which was accessed through the ChemShell [41] package using the CHARMM22 force field [50, 51]. An electronic embedding scheme was adopted in the QM/MM calculations with the MM point charges being incorporated into the one-electron Hamiltonian during the

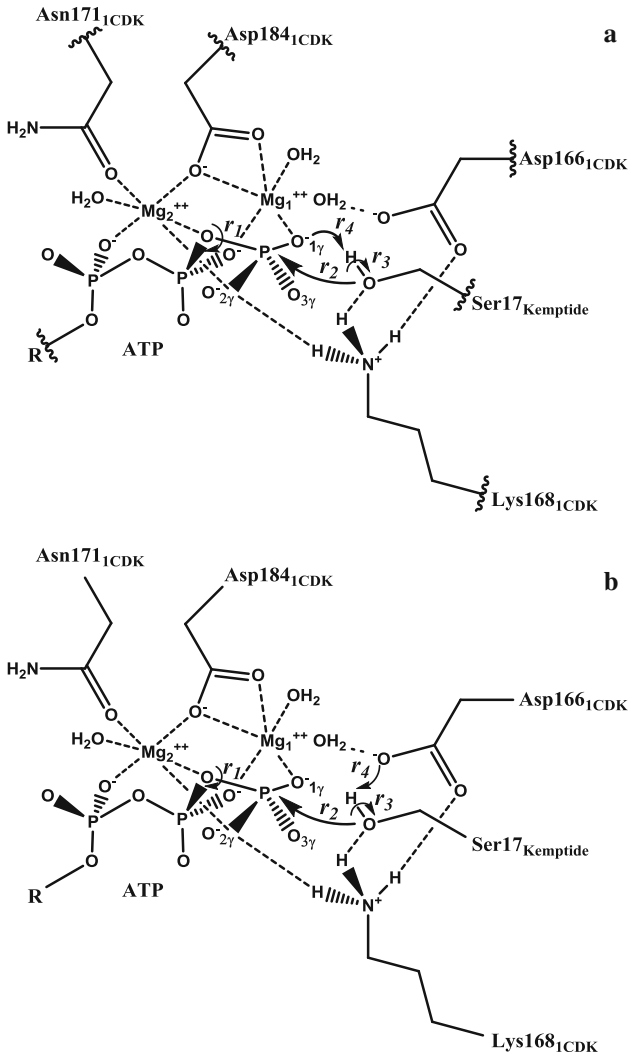

Fig. 2 PKA active site and scheme of the catalytic mechanisms. **a** Associative: all QM atoms are represented, except for the hydrogen atoms of the side chains. The *wavy lines* represent the frontier between QM and MM region (QM/MM electronic embedding scheme), employing hydrogen link atoms to cap the bonds crossing into the MM region (charge shift model). **b** Dissociative (for comparison purposes)

QM calculation. No cutoffs were introduced for the non-bonding MM and QM/MM interactions. The QM/MM boundary has been treated with the charge shift model so, according to the QM region defined below, six hydrogen link atoms were employed to cap the bonds crossing into the MM region [52, 53].

The QM region comprises 65 atoms. It is constituted of two magnesium ions, all the residue side chains and water molecules coordinating them, the complete phosphate tail of the ATP molecule, the Lys168 side chain, that of Asp166 and, obviously, the Ser17 side chain of Kemptide. The total charge of the QM region was −1. A schematic representation of the core is depicted in Fig. 2.

First, the chosen initial structures were fully optimized at the B3LYP/6-31+G(d)/CHARMM level of theory in order to avoid any distorsion provoked by the force field used along the MD simulations and to eliminate any artifact related with each structure. Afterwards, reaction paths were scanned by performing constrained optimizations along a properly defined reaction coordinate R4 in steps of 0.2 Å. This reaction coordinate involves the two antisymmetrical combinations of the bonds to be broken and formed:

$$R4 = r_1 - r_2 + r_3 - r_4 \quad (1)$$

where r_1 is the O3$_\beta$ATP–PγATP distance, r_2 is the OγSer17–PγATP distance, r_3 is the OγSer17–HγSer17 distance, and, finally, r_4 is the HγSer17–O*i*γATP distance (see Fig. 2). The reaction paths have been calculated forward and backward (from reactants to products and vice versa) several times, until the convergence has been reached, i.e. until the potential energy profile of one reaction path and that of the next one were the same.

The foregoing provides starting structures for subsequent full optimization of all relevant stationary points, employing the Limited-memory Broyden-Fletcher-Goldfarb-Shanno (L-BFGS) [54] algorithm in the case of minimizations and the microiterative optimizer combining both the partitioned rational function optimizer (P-RFO) [55] and L-BFGS during the transition state search. All these algorithms are implemented in the HDLCopt [56] module of ChemShell [41]. Frequency calculations on the QM region confirmed that all reported transition states are characterized by a single imaginary frequency and a suitable transition vector that corresponds to the investigated reaction. For more accurate energy evaluations, we performed single point energy calculations at the MP2/cc-pVTZ/CHARMM and the MP2/aug-cc-pVTZ/CHARMM levels of theory. Zero-point energy is not included in the energy values provided in this paper.

Natural population analysis (NPA) [57] charges were determined from QM/MM calculations with QM = B3LYP/6-31+G(d), and applied in a charge balance hypothesis calculation. Also, the contribution of different residues to the QM/MM energy in the associative mechanism was evaluated by setting their point charges to zero in additional energy calculations at the corresponding stationary points. The VMD [58] and CHIMERA [59] programs were used to generate the drawings showing molecular structures.

Moreover, in order to shed more light on the functioning of kinases, we use a MD-generated structure from a previously built model based on the 1CDK crystal structure and the Kemptide substrate [35], in which the residue Asp166 was modified to an alanine, i.e. the D166A model, and the methodology described above was carried through again. In this case, since only the associative mechanism is

feasible and there is no $O_{\delta}i$Asp166–O_{γ}Thr201 distance, the other geometric parameter (besides the O_{γ}Ser17–P_{γ}ATP distance) to consider when defining the MD-frame that could serve as starting point of the QM/MM calculations was the H_{γ}Ser17–Oi_{γ}ATP distance. Therefore, just one MD-frame for this system was selected, namely D166A-eq71 (with 5,069 and 3,599 free and fixed atoms, respectively). As the M1 geometry for the wild type 1CDK model, this selected geometry entailed Thr201 residue side-chain close to the reaction core, interacting mainly with Lys168 ε-amino group.

Results and discussion

As mentioned in the Introduction section our aim in the present work is to shed additional light on the mechanistically relevant interactions found around the P-site residue that might make possible the associative mechanism. That is, the chemical step by which a H atom from the serine residue (Ser17) of the substrate Kemptide goes directly to one of the γ-oxygen atoms of the ATP molecule along the phosphorylation step. We have modeled such a chemical process within the active site cleft of PKA, taking the PDB structure 1CDK as initial crystallographic structural model for PKA.

It has to be noticed that, in a favorable geometry for such chemical process, the H_{γ}Ser17 will point towards one of the three OγATP atoms, which can be distinguished by taking into account their chemical environment (see Fig. 1). Thus, O1γATP coordinates the Mg_1^{2+} ion –referred to as activating–; O2γATP coordinates the Mg_2^{2+} ion –termed inhibitory–[60] and interacts with the positively-charged ε-amino group of Lys168; and, finally, O3γATP points towards the Gly-rich loop (1CDK residues from 52 to 55), but mainly interacts with the side chain hydroxyl group of Ser53.

Thus, for each initial structure selected in this work to model the wild type and the D166A mutant systems, we have simulated the γ-phosphoryl- and the proton-transfers between the ATP molecule and the $Ser17^{Kemptide}$ substrate with each one of the three different γ-oxygen atoms acting as the proton acceptor.

To accomplish this, starting from a configuration conducive to form the HγSer17–OiγATP (i = 1–3) hydrogen bond, full structural optimization on the B3LYP/6-31+G(d)/MM potential energy surface was performed in each case. Then, a potential energy profile has been calculated at the same level of theory as a function of the *R4*-reaction coordinate (defined in the Methods section). That is, performing a sequence of geometry optimizations with a harmonic restraint applied on the *R4*-reaction coordinate, the system was driven from the reactant state, over the reaction barrier, to the product state. At each given restrained value of the *R4*-coordinate, the rest of the QM region and the MM system were optimized. To reduce hysteresis effects, the *R4*-reaction coordinate was explored forward and backward several cycles until the one-dimensional energy curve reached convergence (i.e. until they differ by <0.1 kcal/mol). All the calculated potential energy profiles are represented in Fig. 3.

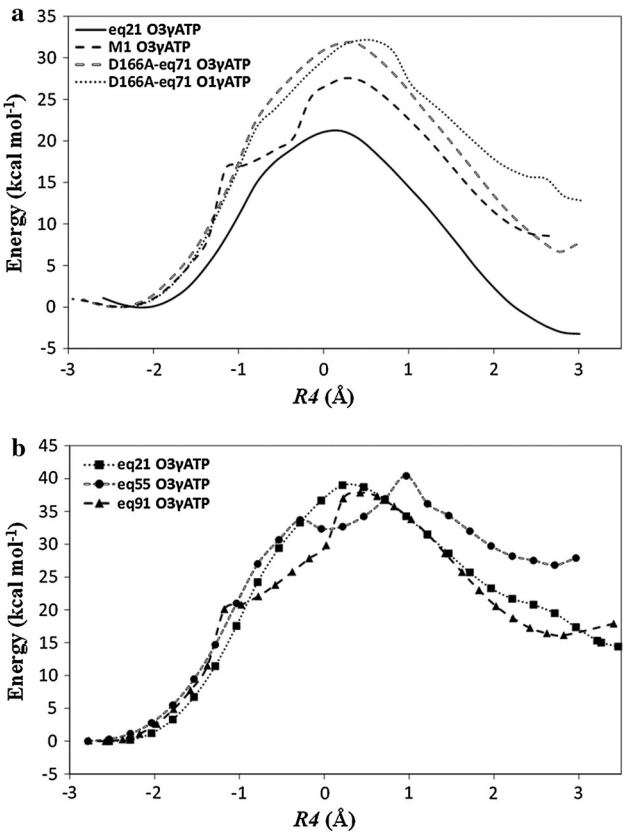

Fig. 3 B3LYP/6-31+G(d)/CHARMM potential energy profiles along the *R4*-reaction coordinate for the phosphoryl transfer step in the PKA model systems via the associative mechanism. **a** Results corresponding to the models that give the lowest potential energy barriers for the wild type system (built from geometries eq21 and M1) and for the D166A mutant model (from eq71), with different O_{γ}ATP atoms as the H_{γ}Ser17 acceptors. **b** Other models for the wild type system that result in higher potential energy barriers

It is worth mentioning that, with respect to our previous theoretical study of the phosphoryl-transfer catalytic mechanism of protein kinase A [20], a more comprehensive approach is taken in this work, since we have made use of the extensive functionality provided by the ChemShell computational chemistry environment. This code has allowed us to model the associative mechanism with a more representative *R4*-reaction coordinate than the one used in our previous work [20]. Here, we have not needed to use fractional coefficients within the *R4*-equation, coefficients that must be further refined through trial and

error assays. Moreover, it has not been necessary to decompose the *R4*-reaction coordinate into simpler *R2*-reaction coordinates to explore the corresponding 2D-potential energy surfaces.

Specifically, Fig. 3a shows the converged potential energy profiles obtained from the initial geometries eq21 and M1 with O3γATP as the proton acceptor atom. It also shows the converged potential energy profiles obtained from the eq71 geometry of the D166A mutant model system with both O1γATP and O3γATP as the proton acceptor atoms. The potential energy barriers obtained for the wild-type models are 21.3 and 27.5 kcal/mol, respectively. For the D166A mutant system, the obtained potential energy profiles depict maxima of 31.8 and 32.1 kcal/mol for the simulations with the O3γATP and the O1γATP atoms as proton acceptors, respectively.

Figure 3b shows the results obtained for other models that result in higher potential energy barriers. Two profiles correspond to the results obtained from geometries eq21 and eq55 of the wild-type enzyme system and with the O1γATP atom involved as proton acceptor, and they indicate that the potential energy maxima are of approximately 40 kcal/mol. The third profile indicates that starting from the eq91 geometry and with the O3γATP atom as proton acceptor, a potential energy maximum of approximately 38 kcal/mol is obtained.

On the other hand, it is worth mentioning that for all initial geometries employed when modeling the associative mechanism with O2γATP as the proton acceptor, the *R4*-reaction coordinate collapses around the expected *R4* values for the transition state ($-0.5 < R4 < +0.5$). This results in a set of distorted geometries with long PγATP-OγSer17 distances, in which the HγSer17-O2γATP bond-forming interaction disturbs the O2γATP coordination to the so-called inhibitory Mg^{2+} ion, and also prevents the existence of the O2γATP–NζLys168 hydrogen-bonding interaction. Being Lys168 an important residue of the catalytic loop to which it has been attributed a role in peptide binding and also in neutralizing the negative charge that develops during the phosphoryl transfer from ATP to the substrate residue [18, 20, 33], the absence of the O2γATP–NζLys168 interaction in such geometries is consistent with the observed incapability of those reactants for reaching a catalytically competent configuration.

Moreover, regarding the simulations with O1γATP as the proton acceptor, it should be noted that from eq91 and M1 the phosphoryl transfer product is not reached. This is a consequence of the unexpected HζLys168 abstraction by the OγSer17 Kemptide atom which in turn prevents the nucleophilic attack on PγATP and causes the deviation of the reaction coordinate prior to reach *R4* values of the transition state region. This result can be rationalized based on the importance of the Asp166–Lys168–Thr201 triad in the active site: the long Asp166–Thr201 distance (approximately 4.2 Å), in the eq91 and M1 initial geometries of the wild type models suggests that the Thr201 residue is not in a suitable position for catalysis, which provokes the loss of its interactions with NζLys168 and OγSer17 along the reaction. Eventually, this also results in a strengthening of the other active site interactions, that is, the gradual shortening of the OγSer17–NζLys168 distance and the consequent improper HζLys168 abstraction by the nucleophilic OγSer17 atom.

Referring to the results with O3γATP as the HγSer17 acceptor, it is interesting to point out that eq55 is the only starting wild type geometry that does not successfully reach the products. In this particular case, from the beginning of the *R4*-reaction coordinate simulation the $O_{\delta i}$Asp166–O_{γ}Thr201 distance drastically decreases from 3.5 to 2.8 Å, and this is accompanied by an increase of the distance from residue Lys168 to the Ser17 substrate residue (but neither to the γ-phosphoryl of the ATP molecule nor to the Asp166 residue). Therefore, as the simulation moves towards the transition state structure region, the increasingly distant and positively-charged ε-amino group of Lys168 is unable to partially neutralize the negative charge that must necessarily be developed on the OγSer17 atom for its nucleophilic attack to the PγATP atom. As a consequence, the simulation cannot approach a product state configuration.

Based on the potential energy profiles presented in Fig. 3, the corresponding reactant Michaelis complex structures were obtained by means of full structural optimization of the lowest-energy geometry of each profile. The same procedure, but with a product-like geometry ($R4_{1CDK} \geq 2.5$ Å, i.e. the ADP/phosphorylated-substrate region) as starting point, was used to localize an associative product structure for each reaction model.

Finally, the structures corresponding to the energy maximum of each reaction profile depicted in Fig. 3 were used as the starting point to locate the corresponding TS structures (see "Models and methods" section). The calculated potential energy differences between the localized stationary points (reactants, transition states and products) are listed in Table 1. From a methodologically point of view, the results in Table 1 suggest that the exploration of the *R4*-reaction coordinate forward and backward is a possible way to obtain a converged and smooth curve which provides suitable starting points for the direct location of the stationary points involved in the reaction.

Hereinafter we present and discuss the results for the associative mechanism of the wild type system with the O3γATP as the proton acceptor because the computed energy barriers given in Table 1 clearly favor these reaction channels over those obtained with O1γATP. In summary, within the associative mechanism, the HγSer17

Table 1 Potential reaction energies (ΔV_R) and barriers ($V^{\neq}$) (in kcal/mol) for the different models of the wild type and D166A mutant enzyme at the B3LYP/6-31+G(d)/CHARMM level. Imaginary frequencies of the transition states are given in parentheses

	O1γATP		O3γATP	
	$V^{\neq}$	ΔV_R	$V^{\neq}$	ΔV_R
eq21 (*wt*)	39.0 (204i)	14.4	21.3 (70i)	−3.2
eq55 (*wt*)	40.2 (74i)	26.6	–	–
eq91 (*wt*)	–	–	37.9 (144i)	16.1
M1 (*wt*)	–	–	27.6 (70i)	8.5
eq71 (D166A)	32.1 (73i)	8.9	31.7 (123i)	4.5

Table 2 Potential energy barriers ($V^{\neq}$) and potential reaction energies (ΔV_R) corresponding to the MP2/cc-PVTZ/CHARMM single-point calculations on the B3LYP/6-31+G(d)/CHARMM stationary points for the wild type and D166A mutant models of the associative mechanism

	$V^{\neq}$	ΔV_R
$eq21_{O3\gamma ATP}$ (*wt*)	19.0	−4.8
$M1_{O3\gamma ATP}$ (*wt*)	24.5	7.8
eq71 ($D166A_{O3\gamma ATP}$)	29.1	7.4
eq71 ($D166A_{O1\gamma ATP}$)	30.7	19.4

Energies are given in kcal/mol

transfer to O3γATP is favored over those to O1γATP and O2γATP, because the first transfer causes the remaining γ-phosphoryl negative charge to accumulate in the O1γATP and O2γATP atoms, where it is more readily stabilized by means of the already existing coordination interactions with the Mg^{2+} ions. In addition, with the O3γATP atom as the proton acceptor, the system only loses the stabilizing interaction of this γ-oxygen of ATP with Ser53 hydroxyl group, without disturbing the coordination sphere of the two Mg^{2+} ions (for which a key role has been suggested) in the nucleotide binding site.

Even more specifically, we will analyze the results obtained for the wild-type eq21 and M1 models because there is a significant difference between their computed potential energy barriers, whose values are 21.3 and 27.6 kcal/mol, respectively. However, before focusing on these two models, it is important to remark that the higher potential energy barrier (37.9 kcal/mol) obtained with the eq91 model, can be explained in terms of a shorter (approximately 0.2 Å) PγATP–OγSer17 distance at the transition state configuration in comparison to the eq21 model, combined with the shift of Ser17 away from the Asp166–Lys168–Thr201 triad all along the simulated reaction path. This last fact is particularly noticeable for Lys168, whose negative charge neutralizing role within the reactive core—as the γ-phosphoryl group passes from ATP to substrate serine—is diminished in this particular case.

Concerning the D166A mutant system, to be able to explain the residual activity shown by the D166A mutant of PKA in terms of the associative mechanism, the results with both the O3γATP (potential energy barrier of 31.7 kcal/mol) and the O1γATP (potential energy barrier of 32.1 kcal/mol) as HγSer17 acceptors, would be considered here because, the two chemically-distinguishable reaction channels are energetically equivalent.

In view of Fig. 3 and Table 1, it is clear that the highlighted models (eq21 and M1) are energetically very different: for the eq21 model the reaction process is exergonic (with the product state located 3.2 kcal/mol below the reactant state), while for the M1 model it is endergonic (with the product state located 8.5 kcal/mol over the reactant state). For the D166A mutant system models endergonic reaction profiles are also obtained, with an average potential reaction energy value of 7 kcal/mol. These differences in the results can be explained in terms of the transferred γ-phosphoryl group interactions and their evolution along the reaction profile and at the product state region.

To complete the energetic analysis we have performed single-point energy evaluations at the MP2/cc-pVTZ/CHARMM level of theory on the B3LYP/6-31+G(d)/CHARMM stationary points of the selected wild type and D166A mutant models (see Table 2). In all cases, the higher level potential energy barriers are lower than the DFT ones. Concerning the wild type models, both potential energy barriers overestimate the phenomenological free energy barrier of 13.7 kcal/mol (derived from the experimental k_{cat} value of 500/s at 296 K and pH 7 [4, 61]. However, in that free energy barrier the contribution of the more favorable dissociative mechanism is included. In any case, the result at the MP2/cc-pVTZ/CHARMM level for the eq21 model that gives the lowest potential energy barrier, among the different selected structures, supports the plausibility of the associative mechanism. Moreover, when single point energy calculations at the MP2/aug-cc-pVTZ/CHARMM level were carried out for this model the potential energy barrier went down to 17.5 kcal/mol. In the same direction, when analyzing the two reaction coordinates simulated for the D166A mutant model, the single-point MP2 results help to explain the residual activity shown by the D166A mutation of PKA (0.4 % of the wild type specific activity in yeast PKA) [24] in terms of the associative mechanism.

Interaction distances analysis

The main structural changes taking place as the reaction goes from reactants to products through the transition state structure involve the motion of the γ-phosphoryl group of

Table 3 Selected B3LYP/6-31+G(d)/CHARMM interaction distances (in Å) for the catalytic core in the optimized reactant Michaelis complex (R), transition state (TS), and product (P) structures for the energetically relevant wild type and D166A mutant models

	eq21 (*wt*; O3γATP)			M1 (*wt*; O3γATP)			eq71 (D166A; O1γATP)			eq71 (D166A; O3γATP)		
	R	TS	P	R	TS	P	R	TS	P	R	TS	P
Interaction distances involved in R4												
$O3_{\beta}ATP–P_{\gamma}ATP$	1.75	1.79	2.83	1.75	1.81	2.79	1.71	1.79	3.97	1.72	1.79	2.89
$P_{\gamma}ATP–O_{\gamma}Ser17$	3.14	2.32	1.66	3.39	2.30	1.69	3.29	2.26	1.65	3.33	2.22	1.65
$O_{\gamma}Ser17–H_{\gamma}Ser17$	0.99	1.66	2.83	0.99	1.73	2.50	0.99	1.96	2.83	0.99	1.72	2.93
$Oi_{\gamma}ATP–H_{\gamma}Ser17$	1.77	1.01	0.99	1.77	1.00	0.99	1.78	0.98	0.98	1.80	1.00	0.99
Catalytic core interaction distances												
$O_{\gamma}1Thr201–O_{\delta}1Asp166$	2.66	2.67	2.64	4.08	4.07	3.98	–	–	–	–	–	–
$O_{\gamma}1Thr201–N_{\zeta}Lys168$	2.73	2.74	2.74	2.76	2.78	2.74	3.04	2.79	2.78	2.98	2.77	2.83
$O_{\gamma}1Thr201–O_{\gamma}Ser17$	4.28	4.56	4.31	4.04	4.44	4.37	3.94	4.09	3.44	3.11	4.01	3.86
$O_{\delta}2Asp166–O_{\gamma}Ser17$	3.78	3.71	3.03	4.22	3.83	3.48	–	–	–	–	–	–
$O_{\delta}2Asp166–P_{\gamma}ATP$	4.27	4.22	3.68	4.20	4.16	3.74	–	–	–	–	–	–
$O_{\delta}2Asp166–OH2^{536}_{XWAT}$	2.96	2.87	2.84	2.70	2.65	2.70	–	–	–	–	–	–
$O_{\delta}2Asp166–N_{\zeta}Lys168$	2.81	2.86	2.89	3.54	3.54	3.52	–	–	–	–	–	–
$O_{\delta}1Asp166–N_{\zeta}Lys168$	3.36	3.42	3.29	2.77	2.86	2.75	–	–	–	–	–	–
$N_{\zeta}Lys168–O_{\gamma}Ser17$	2.75	2.62	2.81	2.76	2.63	2.81	3.62	2.81	3.04	3.04	2.75	3.03
$N_{\zeta}Lys168–O2_{\gamma}ATP$	3.11	2.97	3.56	3.44	3.17	3.17	2.76	3.05	2.91	2.80	3.11	2.71

ATP, the side chain of the substrate serine, and the Mg_2 ion (see Fig. 1), in agreement with the results obtained by Valiev et al. [31] for a dissociative reaction pathway in their PKA model. In this case, though, depending on the model from which the associative mechanism is simulated, there is a noticeable rearrangement of the catalytic core, mainly involving the relative position of Lys168 side chain.

The key bond distances of the B3LYP/6-31+G(d)/CHARMM reactant, transition states, and products structures are listed in Table 3. The changes in the distances between the reactive atoms along the reaction paths indicate that in all models the simulated phosphoryl transfer mechanism has, as expected, a highly associative character.

In particular, from the calculated geometry for the transition state of both eq21 and M1 wild type models, we can see that the distances between the γ-phosphorus and the leaving and entering oxygens are 1.8 and 2.3 Å, respectively. This means that the β–γ phosphoanhydride bond of ATP breaks late in the reaction and the nucleophilic attack of OγSer17 on PγATP occurs when the O3βATP–PγATP bond is, for all practical purposes, still formed (the equilibrium distance is 1.7 Å in the reactant Michaelis complex structures). In this respect, the O3βATP–PγATP interaction distance is almost the same in the transition states structures localized for both the wild type and mutant models, and the same can be established for the length of the nascent PγATP–OγSer17 regardless of which γ-phosphoryl oxygen, O1γ or O3γ, acts as the proton acceptor. Furthermore, it is clear that to increase the nucleophilicity of OγSer17, the HγSer17 transfer from the substrate hydroxyl group to the corresponding oxygen atom of the terminal γ-phosphoryl of ATP must happen prior the transition state configuration is achieved.

The comparison between the enzyme-ligand interaction distance values in the second and third columns of Table 3 indicates that the structural parameter that clearly distinguishes eq21 from M1 model all along the simulation is the Oγ1Thr201–Oδ1Asp166 distance. Results in Table 3 indicate that along the entire simulated paths, the Oγ1Thr201–Oδ1Asp166 distance is 1.4 Å shorter in model eq21 than in model M1, the former being that of a lower potential energy barrier (see Table 2).

Specifically, we have observed a dependence of the Asp166 side chain orientation with respect to the substrate Ser17 and the enzyme Lys168 residue side chain positions when varying the length of the Oγ1Thr201–Oδ1Asp166 interaction: in the eq21 simulated path, Oδ1Asp166 remains further away from the ε-amino group of Lys168 than it does in the M1. That is because in M1 the Oδ1Asp166 practically does not interact with Oγ1Thr201, but does so and strongly with NζLys168 (see Oδ1Asp166–NζLys168 distance in Table 3). Obviously, the last interaction modifies the position of the other carboxylic oxygens in Asp166 side chain, namely Oδ2Asp166, which results in a longer Oδ2Asp166–OγSer17 and Oδ2Asp166–NζLys168 distances. Contrarily, the Oδ2Asp166–PγATP

distance is practically equal in both models; but overall, we can say that in the M1 model, the Asp166 side chain slightly distances from the reaction core region. In addition, Oδ2Asp166 interacts strongly with the conserved water molecule $XWAT^{536}$ through a hydrogen bond, this being stronger for the M1 model along the entire reaction path. As it has been established [31], this interaction occurs as a result of the direct coordination of $XWAT^{536}$ molecule to the Mg1 ion, which activates the hydrogen bond donor properties of the water molecule through strong polarization.

In the results presented here for the associative mechanism, the presence of short hydrogen bond interactions between the Lys168 side chain and both the γ-phosphate and the hydroxyl group of the substrate serine (last two rows in columns 2 and 3 of Table 3) suggests a possible contribution of Lys168 residue in the catalytic process. That is, Table 3 shows that from the reactants to the transition state structure of the wild type associative reaction paths (i.e. eq21 and M1), the positive ε-amino group of Lys168 approaches to the Ser17 residue of the substrate Kemptide and to the ATP molecules, while keeping practically a constant distance with all the rest of residues within the catalytic core. However, in the product region, it comes back to a configuration similar to the initial one. Being the positioning of the γ-phosphate critical for catalysis, it is very significant that Lys168 is the catalytic-loop residue that directly interacts with one of the γ-phosphate oxygen atoms along the phosphoryl transfer, and remains close to the hydroxyl group of the substrate serine, even strengthening these interactions as the reaction proceeds to the transition state configuration. This can be explained by the Lys168 role in neutralizing the negative charge developed in the course of catalysis. Particularly, the nascent and rapidly increasing negative charge in OγSer17 atom during the early proton transfer from the serine residue to the γ-phosphate of ATP. Further, in the transition state, the OγSer17 must perform a nucleophilic attack on the γ-phosphorous atom of ATP, which is surrounded by negatively-charged oxygen atoms. Hence, for the associative mechanism of PKA, the Lys168 side chain is essential in making the nucleophilic attack easier by facilitating the correct orientation of the catalytic/reactant molecular entities (i.e. it plays significant role in binding of the reactants and keeping them in close contact conformation) but also by reducing the repulsion between the negative moieties that must come close for the reaction to be able to happen. In agreement with the catalytic role of Lys168, the mutant K168A had shown a significant reduction of the catalytic activity [24].

When comparing the above results with those we have obtained for the D166A mutant system, we observe (also in Table 3) that almost the unique interaction distance that differs is the Oγ1Thr201–OγSer17 one, which is clearly different all along the simulated profiles (0.5 Å lower in D166A simulations than in the wild-type ones, approximately), together with the NζLys168–OγSer17 distance that is slightly longer in the D166A mutant. Specifically, in the transition state structures obtained for the D166A mutant models, all interactions of NζLys168 in Table 3 but NζLys168–OγSer17 distance are equal to the calculated ones for the wild type saddle points. Thus, in the D166A simulations, the Lys168 side chain starts moving away from ATP while approaching both Ser17 and Thr201 hydroxyl groups, but it does not get that close to the substrate serine as in the wild type models.

Now, we will discuss the results summarized in Table 4, with regard to the residues included in the conserved core of the catalytic domain. Our results indicate that the Mg1 metal ion coordination shell is octahedral, consisting of a chelation interaction by 2β- and 1γ-oxygens of ATP, the Asp184 side chain in a bidentate fashion, and two conserved water molecules. As we have mentioned above, one of these water molecules forms a strong hydrogen bond with Asp166 (see Table 3). This coordination scheme remains almost unchanged all along the reaction process (especially from the reactants to the transition state), what supports the importance of the Mg1 metal ion in nucleotide binding and in properly orientating ATP with respect to the substrate hydroxyl group [31, 60].

On the other hand, in all the stationary point structures localized in this work, the Mg2 metal ion presents a distorted-octahedral coordination sphere, rather than an incomplete fivefold coordination as indicated by X-ray and kinetic measurements [4, 13, 22]. This Mg^{2+} ion binds to the 2α-, 3β- and 2γ-oxygens of ATP, to a single carboxyl oxygen of Asp166, and to the side chain carbonyl oxygen of Asn171. Particularly, the Mg2–O3βATP interaction distance, which almost remains constant from the reactant (2.33 Å) to the transition state (2.28 Å), decreases more than ten percent of its initial value as the reaction proceeds towards the product region (2.03 Å) (Table 4). That is, concomitant with the cleavage of the β–γ phosphoanhydride bond of ATP due the nucleophilic attack of OγSer17 on PγATP, the nascent and leaving ADP moiety is stabilized by the Lewis acid attack of Mg2. The initially weakly bound Mg2 metal ion strengthens its interaction with O3βATP screening in this way the negative charge which progressively accumulates on the β–γ bridging oxygen. In other words, along the associative reaction path, metal ion stabilization of the negative charge accumulation on the β–γ bridging oxygen occurs during the phosphoryl transfer step.

As stated above, within the active site Thr201 anchors both Asp166 and Lys168 via hydrogen bonds to their side chains, such that the results of our study concerning the

Table 4 Selected B3LYP/6-31+G(d)/CHARMM distances (in Å) for the enzyme, nucleotide and metal ions interactions in the optimized reactant (R), transition state (TS), and product (P) structures obtained for the energetically relevant wild type and D166A mutant models

	eq21 (*wt*; O3γATP)			M1 (*wt*; O3γATP)			eq71 (D166A; O1γATP)			eq71 (D166A; O3γATP)		
	R	TS	P	R	TS	P	R	TS	P	R	TS	P
N_{ζ}Lys72–O1$_{\alpha}$ATP	2.76	2.75	2.76	2.72	2.72	2.70	2.74	2.73	2.72	2.75	2.74	2.75
N_{ζ}Lys72–O2$_{\beta}$ATP	2.84	2.87	2.86	2.83	2.84	2.80	2.89	2.87	2.83	2.85	2.86	2.89
N_{ζ}Lys72–O_{ε}2Glu91	2.66	2.66	2.67	2.74	2.72	2.74	2.71	2.71	2.73	2.72	2.72	2.73
O_{γ}Ser53–O3$_{\gamma}$ATP	3.38	3.10	2.64	3.29	2.87	2.61	2.69	2.69	2.65	2.69	2.71	2.65
NSer53–O1$_{\beta}$ATP	2.90	2.81	2.76	2.89	2.81	2.87	2.78	2.78	2.79	2.75	2.73	2.76
NPhe54–O1$_{\beta}$ATP	2.79	2.80	2.77	2.85	2.83	2.84	2.76	2.75	2.80	2.75	2.76	2.79
NGly55–O1$_{\beta}$ATP	2.85	2.89	2.83	2.75	2.79	2.76	>5	>5	>5	>5	>5	>5
Mg ions coordination sphere												
Mg1–O2$_{\beta}$ATP	2.15	2.13	2.07	2.07	2.05	2.00	2.10	2.08	1.95	2.09	2.04	2.03
Mg1–O1$_{\gamma}$ATP	2.02	2.06	2.13	2.03	2.09	2.14	2.05	2.11	3.73	2.12	2.19	2.13
Mg1–O_{δ}1Asp184	2.19	2.19	2.25	2.27	2.27	2.35	2.17	2.20	2.08	2.21	2.12	2.24
Mg1–O_{δ}2Asp184	2.23	2.24	2.19	2.20	2.22	2.16	2.27	2.25	2.23	2.26	2.24	2.24
Mg1–$OH2^{536}_{XWAT}$	2.16	2.14	2.18	2.11	2.08	2.11	2.05	2.07	2.09	2.08	2.07	2.10
Mg1–$OH2^{644}_{XWAT}$	2.06	2.06	2.07	2.14	2.15	2.17	2.06	2.05	2.04	2.04	2.04	2.07
Mg2–O2$_{\alpha}$ATP	2.01	2.01	2.05	2.01	2.02	2.06	2.02	2.03	1.97	2.02	2.02	2.02
Mg2–O3$_{\beta}$ATP	2.33	2.28	2.03	2.25	2.20	2.01	2.34	2.24	1.98	2.28	2.20	1.99
Mg2–O2$_{\gamma}$ATP	2.01	2.04	2.15	2.04	2.09	2.27	2.09	2.08	4.00	2.09	2.09	2.69
Mg2–O_{δ}2Asp184	2.12	2.11	2.12	2.15	2.16	2.14	2.08	2.09	2.14	2.10	2.14	2.08
Mg2–O_{δ}1Asn171	2.01	2.02	2.13	2.03	2.04	2.12	2.03	2.03	2.05	2.05	2.04	2.12
Mg2–$OH2^{551}_{XWAT}$	2.14	2.13	2.14	2.12	2.11	2.12	2.08	2.11	2.08	2.11	2.09	2.11

associative mechanism point towards the fundamental role of Thr201 being the correct spatial positioning of the versatile and catalytically functional Asp166–Lys168–Thr201 triad within the active site during the chemical—phosphorylation transfer—step. In all the simulations carried out with our models, Lys168 bridges the ATP terminal phosphate to the substrate peptide, in a position maintained by its hydrogen bond interaction with the hydroxyl side chain of Thr201.

Electrostatic interaction energy analysis (by residue)

We have calculated the relative electrostatic interaction energy of the MM residues by charge deletion analysis [62, 63] as the phosphorylation reaction proceeds from the reactant to the transition state (based on the B3LYP/6-31+G(d)/CHARMM geometries of the eq21, M1 and D166A mutant models). The results provide a good indication of the enzymatic residues capability in stabilizing or destabilizing the transition state.

Accordingly, the electrostatic interaction energy between a given MM residue and the rest of the QM/MM system was determined with B3LYP/6-31+G(d)/CHARMM single point energy calculations for the reactant and the transition state structures, respectively. The difference between the corresponding reactant state and transition state results indicates the contribution of each residue to the reaction barrier [18]. The residue thus stabilizes the transition state if such difference yields a negative number, and vice versa. The results for the individual MM residues and for the conserved (crystallographic) water molecules within a 10 Å radius sphere from the PγATP atom are shown in Fig. 4 for the different models of the enzyme-substrate system.

Results in Fig. 4a (i.e. wild type models) show that the enzyme and substrate residues surrounding the active site up to 10 Å radius from the ATP γ-phosphorous, have a greater net contribution to the transition state stabilizing through electrostatic interactions in the eq21 model than in the M1 one, as the total accumulated net stabilization effect is of −4.6 and −2.3 kcal/mol, respectively. This result helps to explain the lower energy barrier obtained for the eq21 simulated path. This is mainly due to a considerable catalytic advantage resulting from: (1) the Lys72 interaction with the ATP phosphate tail (detailed below), and (2) from substrate Kemptide residues interactions with enzyme's motifs that directly bind the substrate: principally, with the Gly-rich loop and with the array of anionic Glu residues acting as peptide substrate-PKA enzyme anchorage points (i.e. those located along the small and large lobes that form the conserved core of the catalytic

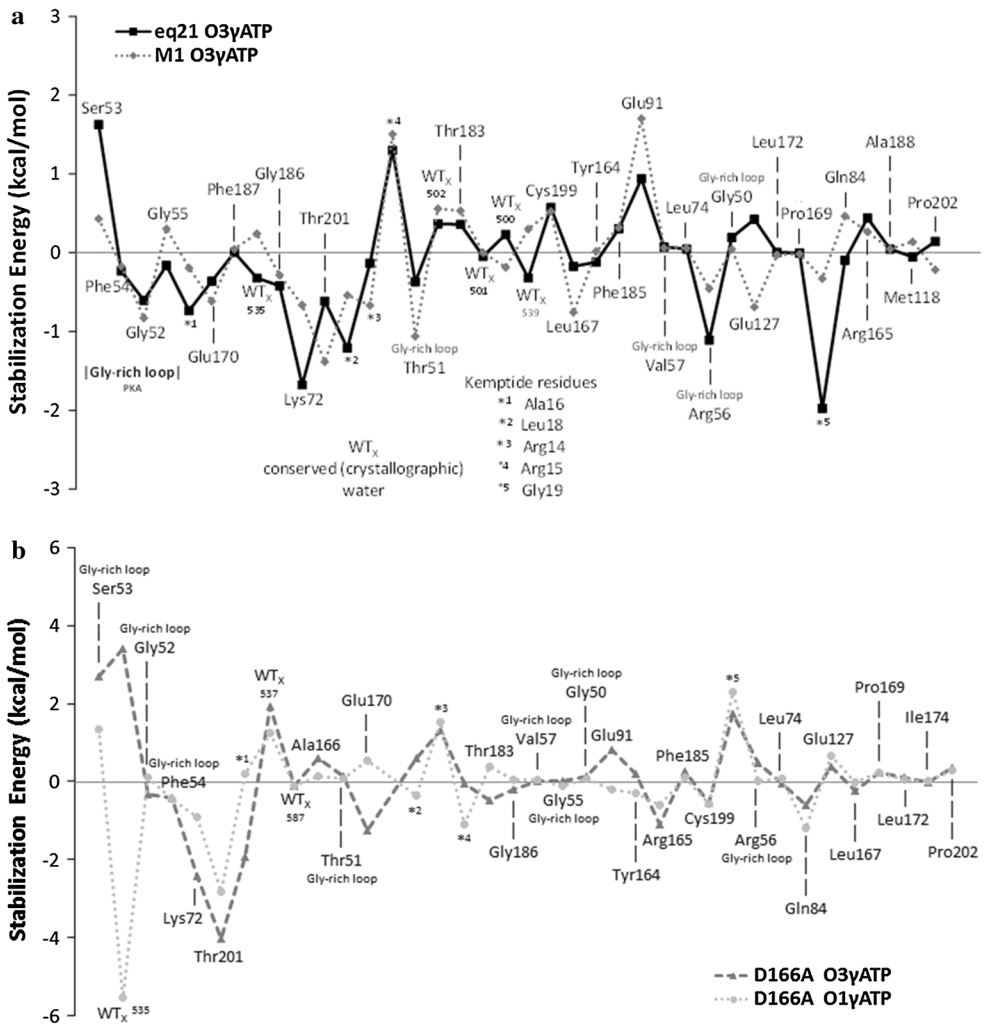

Fig. 4 Individual MM-residue electrostatic contribution to the transition state stabilization and destabilization (residues are ordered as a function to its appearance while moving away from PγATP). **a** eq21 and M1 wild type models (O3γATP as HγSer17 proton acceptor). **b** eq71 D166A mutant models with O3γATP and O1γATP as HγSer17 proton acceptors, respectively

domain). That is, residues in the substrate peptide (some of which bear a charged side chain, as Arg15 and Arg16 do) affect the stabilization of the transition state, so that, to sum up, the overall catalytic effect for the Kemptide residues is to stabilize by 2.8 kcal/mol the eq21 model transition state (in comparison, the net stabilizing effect in the M1 model is 0.2 kcal/mol).

On the other hand, the results in Fig. 4b show that the trends are very similar for all the MM residues in the two D166A mutant models. This analysis suggests a reason why the potential energy barriers calculated for both D166A mutant reaction pathways are almost equal, in contrast to the wild type models where the reactive path with the O3γATP atom as the proton acceptor is clearly favored over that with the O1γATP atom.

The Gly-rich loop, owing to its extended "U" shape spatially aligned with ATP triphosphate tail, is capable of tightly enfolding the nucleotide by means of both hydrogen bonding and hydrophobic interactions. According to Fig. 4, for both wild type and D166A models, out of the eight individual Gly-rich loop residues (50–57) present in our relative interaction energy analysis, only Ser53 exhibits a significant degree of transition state destabilization. In all simulated models, this particular residue interacts via its backbone amide hydrogen with the β-phosphate group and via its side chain hydroxyl oxygen with the γ-phosphate group, specifically with the $O3_{\gamma}ATP$, regardless if the HγSer17 is transferred as a proton to that γ-oxygen of ATP or not (see NSer53-O1βATP and O_{γ}Ser53-$O3_{\gamma}$ATP distances in Table 4, respectively). Experimentally [23], it has been shown that the backbone interaction is the most important, because modifying the side chain scarcely alters the catalytic features of PKA. However, for all our simulation models it is the side chain interaction clearly responsible of setting the terminal phosphate group in the optimal position, thus supporting the essentially structural

role of Ser53. Comparing the results obtained for the wild type models, the higher destabilization in eq21 than in M1 might be due to the larger O_{γ}Ser53–$O3_{\gamma}$ATP distance in the former (see Table 4), so that in the latter the involved hydrogen bond represents a slightly higher stabilizing factor of the transition state. Continuing with the results for the wild type models, the other Gly-rich loop residues show a mild catalytic contribution, with the most prominent transition state stabilization coming from Arg56 residue for the eq21 model and from the Thr51 for the M1 model (although Gly52 also exhibits a significant degree of transition state stabilization in both models). It is noteworthy, however, that for both wild type models almost every residue in the whole loop (with the clear exception of Ser53, as has been noted above) contributes to stabilize the transition state to some degree, indicating a collective influence and a contribution to the lowering of the potential energy barrier; that is, our calculation results indicate that the catalytic role of the Gly-rich loop comes from its effect as a whole, rather than from single residue action. Summing up, the net effect in the wild type models is that the transition state is stabilized by −0.6 kcal/mol in eq21 and −1.7 kcal/mol in M1.

In the D166A models, in addition to Ser53 destabilization, only Gly52 and Phe54 show a small contribution to the transition state stabilization, while the other Gly-rich loop residues practically have no influence at all on this regard. As a consequence, the reaction barrier is increased by 1.1 kcal/mol in the $D166A_{O1\gamma ATP}$ model and by 2.7 kcal/mol in the $D166A_{O3\gamma ATP}$ model.

Lys72 and Glu91 are another two conserved charged residues in the small lobe. Our results indicate that Lys72 anchors α- and β-phosphate and forms a conserved salt bridge with Glu91 (see Table 4). The results in Fig. 4 indicate that Lys72 substantially stabilizes the transition state through electrostatic interactions, whereas Glu91 causes a moderate opposite effect. The stabilization of the transition state by Lys72 is consistent with mutation studies showing that K72A mutation led to an approximate 800-fold decrease in V_{max} with a fivefold increase in K_m (ATP), so that Lys72 facilitates the phosphorylation process without affecting the binding of ATP [24]. Our results indicate that the role of Glu91 is to ensure the proper positioning of the flexible Lys72 side chain in order to maximize its stabilizing interaction with ATP phosphate tail, which in turn might counterbalance Glu91 destabilizing influence. Specifically, in the eq21 wild type model the global contribution of those two PKA conserved residues lowers the potential energy barrier by 0.74 kcal/mol, while in the M1 model a 1.04 kcal/mol destabilizing effect is calculated. Furthermore, in both D166A models the total contributions of Lys72 and Glu91 to lower the potential energy barrier is 1.1 and 1.6 kcal/mol in $D166A_{O1\gamma ATP}$ and $D166A_{O3\gamma ATP}$ models, respectively.

Accordingly to electrostatic transition state stabilization results in Fig. 4, Thr201 encompasses additional potential energy barrier lowering in all wild type and D166A simulated reaction paths. For the wild type simulations, if we take into account that the Thr201 residue is further from Asp166 (see Table 3) in the M1 model than in the eq21 one, and as a consequence the triad Asp166–Lys168–Thr201 is not properly positioned within the active site (which explains the higher energy barrier for the corresponding M1 reaction path), it is surprising that this transition state stabilizing electrostatic contribution is higher for the M1 model. Here, we propose that the foregoing is a result of a more favorable position of Thr201 in the transition state than in the reactant complex, something definitely not observed along the eq21 reaction path, wherein Thr201 keeps a very stable configuration all along the path.

Regarding the D166A models, the Thr201 electrostatic contribution to the transition state stabilization is higher than in the wild type models, probably because in the mutated systems the Thr201–Ser17 interaction is relatively stronger since the Thr201–Asp166 is no longer present. In addition, in Fig. 4b we can see that Thr201 is the residue within the MM region that contributes the most to the electrostatic stabilization of $D166A_{O3\gamma ATP}$ transition state.

Charge balance hypothesis analysis

In order to complete our study on the associative mechanism, the transition state complexes calculated and characterized for the eq21 wild type, M1 wild type, and $D166A_{O3\gamma ATP}$ mutant models have been used to test whether the CBH in the transition state structures regulates enzyme-catalyzed phosphoryl transfer reactions [40].

The charge distribution was calculated by summing the partial charges within a sphere of defined radius centered in the γ-phosphorous atom. For atoms within the QM region we have used NPA charges calculated at the B3LYP/6-31+G(d)/CHARMM level, while for those in the MM region we have used the CHARMM22 parameters. Analysis of the charges in the vicinity of the transition state complexes active site fully supports the adherence of our wild type and mutant magnesium-catalyzed PKA models to the CBH. In Fig. 5, the net charge oscillates around zero charge axes for all models, being the trend and behavior slightly more similar for the wild type M1 and D166A mutant model. This observation is significant when considering the lower potential energy barrier obtained for the eq21 wild type model, which thus, also differs energetically from the other two models. Therefore, the CBH contributes to make possible the nucleophilic attack on a

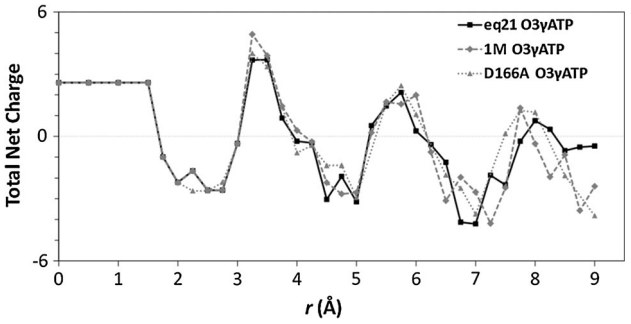

Fig. 5 Charge balance calculation in the active site of the transition state structures localized for the modeled phosphoryl transfer reactions: eq21 wild type model (*solid black line*), M1 wild type model (*dotted square line*), and D166A$_{O3\gamma ATP}$ mutant model (*dotted triangle line*). The charge is summed over all atoms within a sphere of increasing radius *r*, the center of which is the transferring γ-phosphorous

dianionic phosphate group in spite of the Coulombic repulsion involved.

Conclusions

In the work described here we have explored the plausibility of the associative mechanism in the reaction catalyzed by PKA, taking as starting point selected structures obtained in our previous works on this protein kinase. The results obtained in those works already indicated the possible catalytic role of the associative mechanism in the phosphoryl transfer reaction in the mammalian PKA-C enzyme and its D166A mutant, and therefore, reopened a debate that in view of the last theoretical papers in the field seemed to be overcame. That is, recent papers pointed out the dissociative mechanism as the only possible reaction channel for PKA; in spite of the experimental evidence of the existence of residual enzyme activity when this pathway is impeded. We decided to improve the accuracy of our calculations and to complete our analysis of the key points in the associative mechanism to be able to contribute more significantly to the mechanistic discussion of the kinases catalytic mechanism. We focused on two different aspects: the role of individual residues, which has been explored here by means of interaction distances and electrostatic interaction energy analyses, and the transition state stabilization, which has been tested by the charge balance hypothesis.

The potential energy barriers obtained at the DFT/MM and MP2/MM levels of theory support the existence of an associative mechanism channel in the wild type enzyme reaction. In addition, the comparison of the potential energy profiles obtained for the wild type and the mutant enzymes is in agreement with the experimental data.

Our results indicate that the triad Asp166–Lys168–Thr201 is essential for catalysis, something that has been proposed in previous experimental papers, but has hardly been discussed and analyzed in theoretical works.

Finally, the transition state structures localized in our models of the wild type and mutant enzymes accomplish the charge balance hypothesis.

Overall, we think that this paper contributes to advance in the way of finding answers at a molecular level to the most intriguing questions derived from experimental data about the catalytic mechanism of protein kinases in general, and specifically, of PKA.

Acknowledgments This work was supported by the "Ministerio de Economía y Competitividad" through Project CTQ2011-24292 and by the "Generalitat de Catalunya" through Project 2009SGR409. Use of computational facilities at the "Centre de Serveis Científics i Acadèmics de Catalunya (CESCA)" is also gratefully acknowledged. Ayax Pérez-Gallegos acknowledges "Consejo Nacional de Ciencia y Tecnología (CONACYT)" Supporting Grant 213582.

References

1. Cohen P (2002) Nat Rev Drug Discov 1:309–315
2. Johnson L, Noble M, Owen D (1996) Cell 85:149–158
3. Cohen P (2001) Eur J Biochem 268:5001–5010
4. Adams JA (2001) Chem Rev 101:2271–2290
5. Johnson DA, Akamine P, Radzio-Andzelm E, Madhusudan, Taylor SS (2001) Chem Rev 101:2243–2270
6. Francis S, Corbin J (1994) Annu Rev Physiol 56:237–272
7. Smith C, Radzio-Andzelm E, Madhusudan, Akamine P, Taylor SS (1999) Prog Biophys Mol Biol 71:313–341
8. Taylor SS, Kornev A (2012) PKA: prototype for dynamic signaling in time and space. In: Wall ME (ed) Quantitative biology: from molecular to cellular systems. CRC Press, Boca Raton, Fl (USA), pp 267–298
9. Zheng J, Trafny E, Knighton D, Xuong N-H, Taylor SS, Ten Eyck L, Sowadski J (1993) Acta Crystallogr D Biol Crystallogr D49:362–365
10. Masterson L, Shi L, Metcalfe E, Gao J, Taylor SS, Veglia G (2011) Proc Natl Acad Sci USA 108:6969–6974
11. Armstrong R, Kondo H, Granot J, Kaiser E, Mildvan A (1979) Biochemistry 18:1230–1238
12. Shaffer J, Adams JA (1999) Biochemistry 38:12072–12079
13. Adams JA, Taylor SS (1992) Biochemistry 31:8516–8522
14. Bastidas A, Deal M, Steichen J, Guo Y, Wu J, Taylor SS (2013) J Am Chem Soc 135:4788–4798
15. Jacobsen DM, Bao ZQ, O'Brien P, Brooks CL III, Young MA (2012) J Am Chem Soc 134:15357–15370
16. Gerlits O, Waltman M, Taylor SS, Langan P, Kovalevsky A (2013) Biochemistry 52:3721–3727
17. Gerlits O, Das A, Keshwani M, Taylor SS, Waltman M, Langan P, Heller W, Kovalevsky A (2014) Biochemistry 53:3179–3186
18. Cheng Y, Zhang Y, McCammon J (2005) J Am Chem Soc 127:1553–1562
19. Valiev M, Kawai R, Adams JA, Weare JH (2003) J Am Chem Soc 125:9926–9927

20. Montenegro M, Garcia-Viloca M, Lluch JM, González-Lafont À (2011) Phys Chem Chem Phys 13:530–539
21. Madhusudan, Akamine P, Xuong N-H, Taylor SS (2002) Nat Struct Biol 9:273–277
22. Yang J, Ten Eyck LF, Xuong N-H, Taylor SS (2004) J Mol Biol 336:473–487
23. Aimes R, Hemmer W, Taylor SS (2000) Biochemistry 39:8325–8332
24. Gibbs C, Zoller M (1991) J Biol Chem 266:8923–8931
25. Madhusudan, Trafny E, Xuong N-H, Adams JA, Ten Eyck L, Taylor SS, Sowadski J (1994) Protein Sci 3:176–187
26. Bossemeyer D, Engh R, Kinzel V, Ponstingl H, Huber R (1993) EMBO J 12:849–859
27. Skamnaki V, Owen D, Noble M, Lowe E, Lowe G, Oikonomakos N, Johnson L (1999) Biochemistry 38:14718–14730
28. Hart JC, Sheppard DW, Hillier IH, Burton NA (1999) Chem Commun 1:79–80
29. Sheppard DW, Burton NA, Hillier IH (2000) J Mol Struct (Theochem) 506:35–44
30. Hutter MC, Helms V (2003) Int J Quantum Chem 95:479–486
31. Valiev M, Yang J, Adams JA, Taylor SS, Weare J (2007) J Phys Chem B 111:13455–13464
32. Díaz N, Field M (2004) J Am Chem Soc 126:529–542
33. Cheng Y, Zhang Y, McCammon J (2006) Protein Sci 15:672–683
34. Montenegro M, Garcia-Viloca M, González-Lafont À, Lluch JM (2007) J Comput Aided Mol Des 21:603–615
35. Montenegro M, Masgrau L, González-Lafont À, Lluch JM, Garcia-Viloca M (2012) Biophys Chem 161:17–28
36. Krishna SS, Zhou T, Daugherty M, Osterman A, Zhang H (2001) Biochemistry 40:10810–10818
37. Thoden JB, Holden HM (2005) J Biol Chem 280:32784–32791
38. Prasad B, Plotnikov N, Warshel A (2013) J Phys Chem B 117:153–163
39. Lee J, Yang W (2006) Cell 127:1349–1360
40. Jin Y, Cliff M, Baxter N, Dannatt H, Hounslow A, Bowler M, Blackburn G, Waltho J (2012) Angew Chem Int Ed 51:12242–12245
41. Sherwood P, de Vries AH, Guest MF, Schreckenbach G, Catlow CRA, French SA, Sokol AA, Bromley ST, Thiel W, Turner AJ, Billeter S, Terstegen F, Thiel S, Kendrick J, Rogers SC, Casci J, Watson M, King F, Karlsen E, Sjøvoll M, Fahmi A, Schäfer A, Lennartz C (2003) J Mol Struct (Theochem) 632:1–28
42. Ahlrichs R, Bär M, Häser M, Horn H, Kölmel C (1989) Chem Phys Lett 162:165–169
43. Slater JC (1951) Phys Rev 81:385–390
44. Vosko SH, Wilk L, Nusair M (1980) Can J Phys 58:1200–1211
45. Becke AD (1988) Phys Rev A 38:3098–3100
46. Becke AD (1993) J Chem Phys 98:5648–5652
47. Stephens PJ, Devlin FJ, Chabalowski CF, Frisch MJ (1994) J Phys Chem 98:11623–11627
48. Lee C, Yang W, Parr RG (1988) Phys Rev B 37:785–789
49. Smith W, Forester T (1996) J Mol Graph 14:136–141
50. MacKerell AD, Bashford D, Bellott M, Dunbrack RL, Evanseck JD, Field MJ, Fischer S, Gao J, Guo H, Ha S, Joseph-McCarthy D, Kuchnir L, Kuczera K, Lau FTK, Mattos C, Michnick S, Ngo T, Nguyen DT, Prodhom B, Reiher WE, Roux B, Schlenkrich M, Smith JC, Stote R, Straub J, Watanabe M, Wiórkiewicz-Kuczera J, Yin D, Karplus M (1998) J Phys Chem B 102:3586–3616
51. MacKerell AD, Feig M, Brooks CL (2004) J Am Chem Soc 126:698–699
52. de Vries AH, Sherwood P, Collins SJ, Rigby AM, Rigutto M, Kramer G (1999) J Phys Chem B 103:6133–6141
53. Sherwood P, de Vries AH, Collins SJ, Greatbanks SP, Burton NA, Vincent MA, Hillier IH (1997) Faraday Discuss Chem Soc 106:79–92
54. Liu D, Nocedal J (1989) Math Prog 45:503–528
55. Baker J (1986) J Comput Chem 7:385–395
56. Billeter SR, Turner AJ, Thiel W (2000) Phys Chem Chem Phys 2:2177–2186
57. Reed AE, Weinstock RB, Weinhold F (1985) J Chem Phys 83:735–746
58. Humphrey W, Dalke A, Schulten K (1996) J Mol Graph 14(33–38):27–38
59. Pettersen EF, Goddard TD, Huang CC, Couch GS, Greenblatt DM, Meng EC, Ferrin TE (2004) J Comput Chem 25:1605–1612
60. Khavrutskii I, Grant B, Taylor SS, McCammon J (2009) Biochemistry 48:11532–11545
61. Grant B, Adams JA (1996) Biochemistry 35:2022–2029
62. Szarek P, Dyguda-Kazimierowicz E, Tachibana A, Sokalski W (2008) J Phys Chem B 112:11819–11826
63. Garcia-Viloca M, Truhlar D, Gao J (2003) Biochemistry 42:13558–13575